STUDY ON CONCEPTS FOR RADAR INTERFEROMETRY FROM SATELLITES FOR OCEAN (AND LAND) APPLICATIONS

Studie zu Konzepten für Radar-Interferometrie über Ozeanen (und Land) im Rahmen zukünftiger Satellitenmissionen

(KoRIOLiS)

SECTION 4: WAVE MEASUREMENTS

Johannes Schulz-Stellenfleth, Susanne Lehner

4.1. Motivation 4-2
4.1.1. Promising Applications 4-2
4.1.2. Alternatives to InSAR 4-3
4.2. Ocean Wave Fundamentals 4-3
4.3. InSAR Ocean Wave Measurements 4-5
4.3.1. ATI wave imaging mechanism 4-6
4.3.2. XTI wave imaging mechanism 4-6
4.3.3. Hybrid InSAR wave imaging mechanism 4-7
4.3.4. Impact of wave motion 4-7
4.3.4.1. Scanning Distortion 4-7
4.3.4.2. “Train off the track effect” 4-8
4.3.4.3. Quasilinear Transform 4-9
4.3.5. Retrieval Approaches 4-11
4.4. Key Parameters 4-11
4.4.1. Along Track Baseline 4-11
4.4.2. R over V Ratio 4-11
4.4.3. Image Size 4-12
4.5. Simulations of InSAR phase spectra 4-12
4.6. Signal to noise ratio of phase spectra 4-13
4.7. Experimental evidence 4-17
4.7.1. Across track Interferometry 4-17
4.7.2. Hybrid Interferometry 4-17
4.7.2.1. Hybrid two antenna interferometry from space 4-17
4.7.2.2. Airborne three antenna hybrid interferometric measurements 4-19
4.8. SUMMARY 4-22

In this chapter the ability of spaceborne interferometric synthetic aperture radar to provide information on ocean surface gravity waves is discussed. The basic imaging mechanisms are described and the influence of different system parameters as well as geophysical variables are analysed.

The chapter is organised as follows. In section 4.1 the motivation for ocean wave measurements in general and the use of InSAR systems in particular are discussed. In section 4.2 some basic information on ocean waves is introduced, which is needed for the subsequent analysis. Section 4.3 gives an overview over the InSAR ocean wave imaging process of both along-, across-, and combined along/across track systems. In section 4.4 simulations of along-, across- and hybrid interferometric data are performed using typical spaceborne imaging parameters. Section 4.5 is about the analysis of the signal to noise ratio of phase variance spectra, e.g. the question under which circumstances wave systems can be detected in interferometric data. In section 4.6 some results obtained in experiments with airborne InSAR systems are presented. Furthermore the ability of spaceborne InSAR to image ocean waves is demonstrated using data acquired during the Shuttle Radar Topography Mission (SRTM).

4.1. Motivation

Up to now spaceborne SAR is still the only instrument providing two dimensional spectral information on ocean waves on a global and continuous basis. Whereas instruments like the altimeter only estimate waveheight, additional information on wavelength, propagation direction and waveheight of different subsystems is available from SAR. As todays ocean wave models have reached a level of accuracy where further improvements seem to require the assimilation of directional information, the interest in spaceborne SAR systems, e.g. at weather centres is growing.

The use of interferometric SAR systems for ocean wave measurements is a relatively new technique *Shemer & Kit* [1991]; *Goldstein et al.* [94]; *Bao et al.* [1997]; *Schulz-Stellenfleth et al.* [2001]; *Schulz-Stellenfleth & Lehner* [2001a]. Along track interferometry was first used to measure currents *Goldstein et al.* [89]; *Shemer et al.* [1993]; *Romeiser & Thompson* [2000]. The idea of the technique is to use two antennas with a baseline in the along track direction (azimuth) to acquire two complex SAR images with a small time offset. From the phase difference of the images information on the orbital motion of the sea surface can be derived. The orbital velocity is associated with both currents and ocean waves. As the relationship between wave motion and elevation is known along track InSAR data can be used to estimate two dimensional wave spectra.

The use of across track interferometry for direct estimation of sea surface elevation has been analysed in *Schulz-Stellenfleth et al.* [2001]. An experiment with an airborne system is describes in *Schulz-Stellenfleth & Lehner* [2001a].

Compared to conventional SAR imagery both along and across track interferometric data have the big advantage to be much less sensitive with respect to the real aperture radar modulation mechanism which is known only with low accuracy *Brüning et al.* [1994]; *Feindt et al.* [1986]. Furthermore the use of combined along and across track InSAR systems allow simultaneous estimations of sea surface elevation and orbital velocities. This combined information not only leads to even more reliable ocean wave measurements but also gives new insight into geophysical processes like ocean wave current interaction or wave breaking.

4.1.1. Promising Applications

Global and continuous measurement of ocean waves is an important task for different reasons. The most important applications from our point of view are:

- Assimilation of numerical ocean wave models in order to improve wave forecast especially needed for:
  - ship operations
  - off-shore operations
  - harbour protection
- climate change studies

- Tracking and analysis of extreme events, e.g.
  - tracking of swell
  - Investigation of extreme individual waves

In most applications people are increasingly interested in detailed two dimensional spectral information. For instance the prediction of swell with accurate propagation direction, period and waveheight is an important issue for both harbour protection and off-shore operations.

4.1.2. Alternatives to InSAR

As pointed out already there is at the moment no real alternative to spaceborne SAR if directional wave information is required on a global scale. Conventional Synthetic aperture radar has been used for continuous and global ocean wave measurements since the launch of the ERS-1 satellite in 1991. Imaging of ocean waves with these single SAR antennas is mainly based on the modulation of the radar cross section of the sea surface by different geometric and hydrodynamic mechanism *Hasselmann et al.* [1985]. Although these data have been successfully used for wave model assimilation *Breivik et al.* [1998], the accuracy of the estimated wave parameters is limited by stochastic components in the modulation processes *Brüning et al.* [1994]; *Feindt et al.* [1986]; *Romeiser et al.* [1994]. As the accuracy of wave models is further growing it is foreseeable that more accurate measurement systems are required to achieve further improvements in the future.

For applications where knowledge about waveheight is sufficient spaceborne altimeter has turned out to be a reliable instrument, which is used for operational wave model assimilation at weather centres *Lionello et al.* [1992]. However, altimeter provides no information on propagation direction or wavelength.

There are a variety of other ground-based remote sensing instruments like marine radar *Young et al.* [1985] and HF radar *Graber et al.* [1996] as well as in situ instruments like directional waverider buoys, which are capable to measure two dimensional wave spectra. These instruments provide ocean wave measurements on local (buoy) and regional (HF radar) scales and have demonstrated their big potential in particular for monitoring of coastal regions.

4.2. Ocean Wave Fundamentals

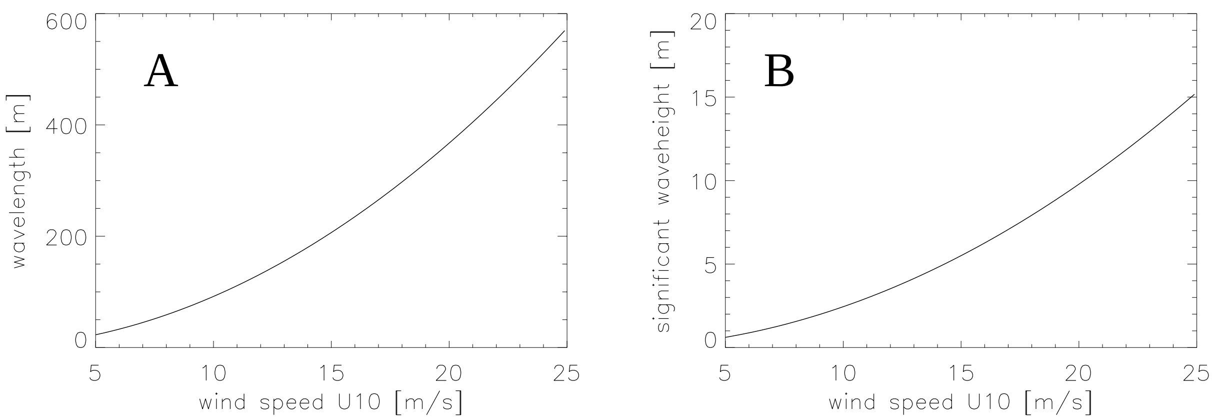

Figure 4-1: Dependence of wavelength (A) and waveheight (B) on wind speed for fully developed wind seas.

Due to their stochastic nature ocean waves are commonly described by statistical parameters. In practice only moments up to second order a taken into account (linear Gaussian wave theory). Denoting the sea surface elevation (with respect to mean sea level) with η one has

$$\langle \eta \rangle = 0 \tag{4-1}$$

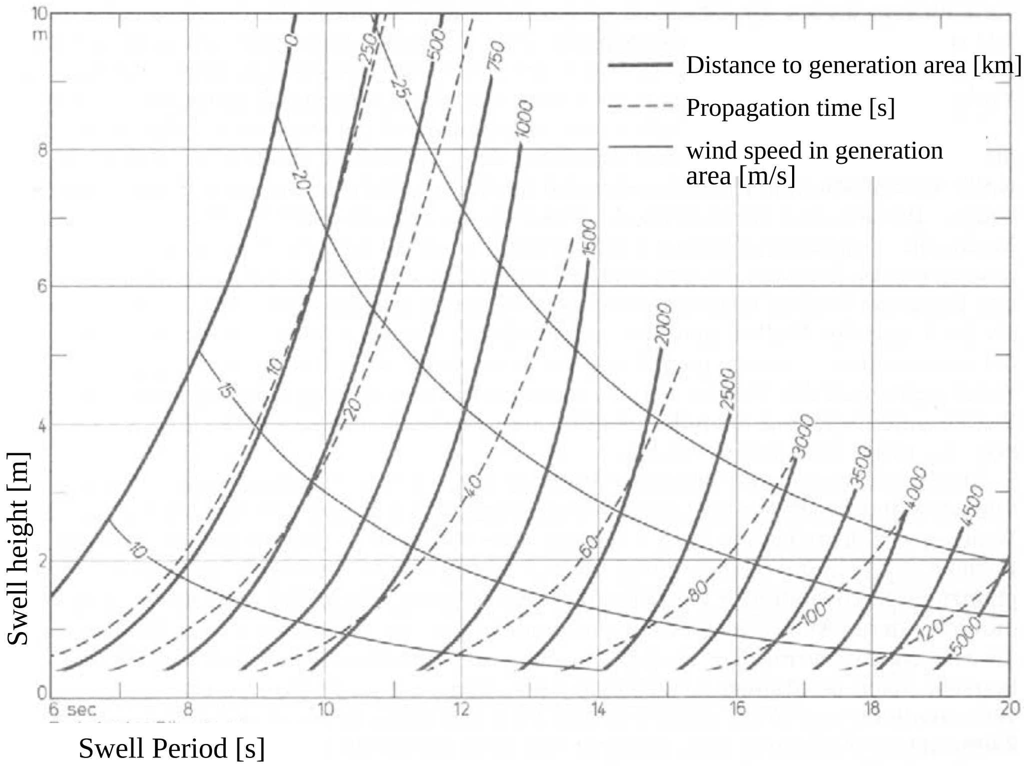

Figure 4-2: Diagram for swell propagation (adapted from Dietrich et al. *[1975])*

for the first moment. The second moments are usually defined based on a Fourier representation of the sea surface elevation field

$$\eta(x,t) = 2\,Re\Big[\int \eta_k \,\exp(i\,(k\,x - \omega\,t)\Big] \tag{4-2}$$

where η_k are the complex Fourier coefficients of η. The two dimensional ocean wave spectrum F is then defined as:

$$F_k = 2\,\langle \eta_k^2 \rangle \tag{4-3}$$

Based on the wave spectrum different useful parameters like the significant waveheight H_s can be defined.

$$H_s = 4\sqrt{\int F_k\,dk} = 4\,\text{stdv}(\eta) \tag{4-4}$$

The waveheight H_s is approximately equal to the average of the 30% highest waves and is consistent with estimates made by ship personal.

Ocean waves are generated by the near surface wind. If the wind is blowing over a long time and a long distance (fetch) a equilibrium sea state is observed which has typical spectral properties depending on wind speed *Hasselmann* [1973]. Fig. 4-1 shows the wavelengths and significant waveheights of fully developed wind seas as a function of wind speed in 10 m height.

The wind generated ocean waves propagate away from the generation area with phase speed

$$c_{Ph} = \sqrt{g/k} \tag{4-5}$$

(assuming deep water) with acceleration of gravity g and wavenumber k [rad]. For example a 100 m wave has a phase speed of about 10 ms^{-1}. Having left the area of generation the wavelengths increases due to nonlinear interactions and the waves become swell. Fig. 4-2 shows a diagram with swell waveheight and period as a function of propagation time, fetch and wind speed. The wave period T is related to wavelength λ (assuming deep water) by:

$$\lambda = \frac{T^2\, g}{2\,\pi} \tag{4-6}$$

For instance a wave with 10 s period has about 150 m wavelength and 20 s corresponds to about 600 m. The diagram shows that in some cases swell of significant amplitude can be observed even several thousand kilometres away from the area of generation.

InSAR systems map a two dimensional ocean wave spectrum into the corresponding phase image spectrum. For the simulations in this study a parametric ocean wave spectrum is used which is based on the JONSWAP model *Hasselmann et al.* [1980]. For the directional distribution we follow *Mitsuyasu et al.* [1975], who introduced a wind and frequency dependent spreading function (see also *Brüning et al.* [1990]).

$$F(k) = \frac{\alpha}{2}\; k^{-4} \exp(-\frac{5}{4}\frac{k^{-2}}{k_m^{-2}} + log\gamma\; \exp(-\frac{(\sqrt{k}-\sqrt{k_m})^2}{2\sigma_j^2\; k_m})N(p)\cos^{2\;p}(\Phi-\Phi_m) \tag{4-7}$$

The model represents a single wave system with peak wavenumber k_m, peak enhancement factor γ and propagation direction Φ_m. The parameter σ_j describes the wavenumber spread of the spectrum

$$\sigma_j = \begin{cases} \sigma_a & \text{if } \; k \le k_m \\ \sigma_b & \text{if } \; k \ge k_m \end{cases} \tag{4-8}$$

while p represents the directional spreading.

$$p = \begin{cases} 0.46\; (k/k_m)^{-1.25}\; p_m & \text{if } \; k \ge k_m \\ 0.46\; (k/k_m)^{2.5}\; p_m & \text{if } k \le k_m \end{cases} \tag{4-9}$$

The parameter p_m is defined as:

$$p_m = 11.5\; (U/c_m)^{-2.5} \tag{4-10}$$

Here U is the windspeed at 19.5 m height and c_m is the phase velocity of the peak wavenumber. $N(p)$ is a normalisation factor given by:

$$N(p) = \frac{1}{\sqrt{\pi}}\; \frac{\Gamma(1+p/2)}{\Gamma(1/2+p/2)} \tag{4-11}$$

For simulations of fully developed wind seas we use $\alpha = 0.0081$ and $\gamma = 1$ in accordance with *Brüning et al.* [1990].

4.3. InSAR Ocean Wave Measurements

In this section the ocean wave imaging mechanism for along, cross-, and hybrid InSAR systems are summarized. In the first step the so called “train off the track” effect is neglected, and only the very basic imaging mechanisms are explained. The impact of the more complicated effects is explained in a second step.

InSAR wave measurements are based on the interferogram i, which is defined as

$$i = \langle c_1\, c_2^* \rangle \tag{4-12}$$

Here, c_1, c_2 are two complex SAR images acquired by the InSAR system, the asterisk denotes complex conjugation and brackets indicate mean quantities. Depending on the antenna geometry the phase Φ of the interferogram is associated with different parameters of the ocean wave field.

4.3.1. ATI wave imaging mechanism

Due to the along track baseline the two complex SAR images c_1, c_2 acquired by an ATI system have a small time offset. Along track InSAR data thus contain information on the orbital velocity of the wave field. The orbital velocities associated with surface gravity waves have about the same order of magnitude as currents (< 3ms^{-1}) discussed in chapter 3. Denoting the slant range component of the orbital velocity with u_r and the along track baseline with B_x the ATI phase associated with the orbital motion is to first order given by:

$$\Phi_{ATI} \quad = \quad m\, k_E\, \frac{B_x}{V}\, u_r =: m\, \frac{2\,\pi}{u_r^{amb}}\, u_r \qquad (4\text{-}13)$$

Here m is a system dependent constant given by:

$$m = \begin{cases} 1 & : \text{ bistatic mode, e.g. one antenna transmits and both antennas receive} \\ 2 & : \text{ monostatic mode, e.g. both antennas transmit and receive} \end{cases} \qquad (4\text{-}14)$$

R_0 is slant range, V is platform velocity, k_E is the electromagnetic wavenumber and θ is the incidence angle. Furthermore we have defined the ambiguity velocity u_r^{amb}, which corresponds to an interferometric phase of 2π. For example the SRTM system *Werner* [2000], which operated in bistatic mode had an ambiguity velocity of about 30 ms^{-1} (C-band data).

The orbital velocity in slant range u_r, which determines the along track interferometric phase (eq. 4-13) can be expressed using the Fourier representation eq. 4-2 as follows:

$$u_r(x) = 2\, Re\left[\int\; \eta_k\, T_k^u\; \exp(i\; k\, x)\; dk\right] \qquad (4\text{-}15)$$

Here, T^u is the slant range velocity transfer function given by *Hasselmann & Hasselmann* [1991]:

$$T_{\mathbf{k}}^u = \omega\,(\sin\theta\; \frac{k_y}{|\mathbf{k}|} - i\; \cos\theta) \qquad (4\text{-}16)$$

where ω is wave frequency, θ is incidence angle, k_y is the range wavenumber component and furthermore we assumed a right looking antenna geometry. This means that at least in the linear approximation there is a simple one to one correspondence between sea surface elevation and orbital velocity. Based on this relationship sea surface elevation fields can be retrieved from along track data.

4.3.2. XTI wave imaging mechanism

Cross track interferometry was originally designed for land application. Airborne and spaceborne InSAR systems have demonstrated their ability to measure high precision digital elevation models (DEMs) of terrain. Airborne systems have reached height accuracies of up to 5 cm under optimal conditions *Wimmer et al.* [2000]. The technique was only recently applied for the measurement of ocean waves.

The two antennas of an cross-track InSAR system image the sea surface at slightly different geometries. Due to this fact the XTI phase contains information on sea surface elevation.

Denoting the sea surface elevation with η and the perpendicular baseline with $B_\perp$ *Bamler & Hartl* [1998] the cross track phase can be written as:

$$\Phi_{xti} \quad = \quad m\, k_E\, \frac{B_\perp}{R_0\; \sin\theta}\, \eta = m\, \frac{2\,\pi}{\eta_r^{amb}}\, \eta \qquad (4\text{-}17)$$

with m as defined in eq. 4-14 and η_r^{amb} defined as the ambiguity height, which corresponds to an interferometric phase of 2π(compare Fig. 2.2.4). For example the SRTM system *Werner* [2000] had an ambiguity height of 180 m (C-band data). Furthermore we have assumed in eq. 4-18 that the phase variations which are associated with the flat surface (fringe frequency) have been removed from the cross track phase according to standard InSAR processing.

4.3.3. Hybrid InSAR wave imaging mechanism

Most real InSAR systems are a combination of along and cross track configurations, e.g. the baselines contain both along and cross track components. This circumstance is often due to pure technical restrictions like in the SRTM case *Werner* [2000]. For airborne systems hybrid geometries are often introduced by squint angles associated with cross wind. We will call these combined ATI/XTI systems hybrid InSAR in the following. For a hybrid system which has a physical along track baseline of length B_x and a perpendicular baseline $B_\perp$ *Bamler & Hartl* [1998] the interferometric phase is given by:

$$\Phi_{hybr} = \Phi_{xti} + \Phi_{ati} \tag{4-18}$$

Here, Φ_{xti} and Φ_{ati} are given by eq. 4-13 and eq. 4-17. A straightforward validation of eq. 4-18 can be found in *Siegmund et al.* [2002], where simultaneous measurements of stationary topography and currents in the Wadden sea were performed.

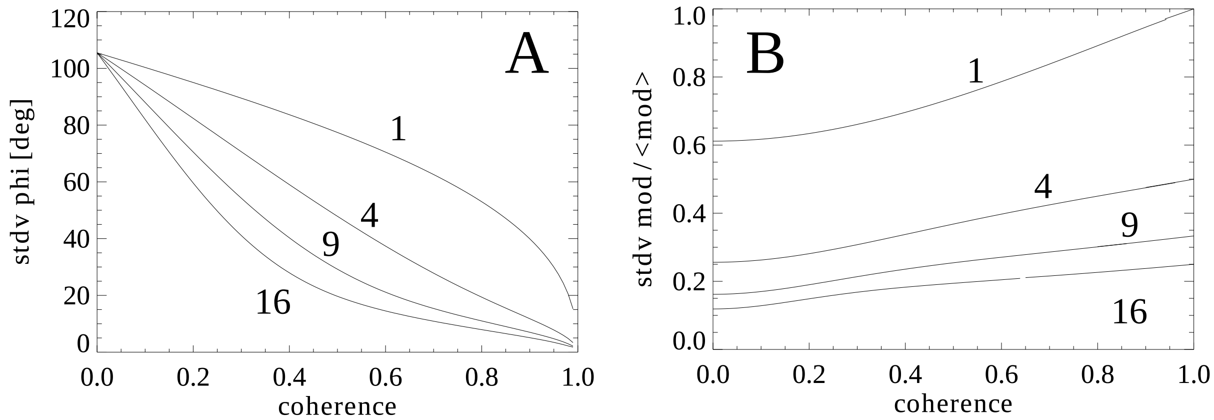

Figure 4-3: Standard deviation of interferogram phase (A) and normalised magnitude (B) as a function of coherence.

4.3.4. Impact of wave motion

For InSAR measurements the ocean wave motion during the acquisitions process has to take into account. In general the first imaging mechanism to be considered in the InSAR simulation process is scanning distortion, which is a shearing of the imaged ocean waves due to the finite radar platform velocity.

4.3.4.1. Scanning Distortion

As the ocean wave phase speed c_{ph} for a given water depth is known theoretically (in this study infinite water depth is assumed), this effect can be readily simulated by applying the following transformation in the spectral domain.

$$k'_x = k_x - \frac{c_{ph}}{V}\,|k| \tag{4-19}$$

$$k'_y = k_y \tag{4-20}$$

Here k_x, k_y are the wavenumber components in range and azimuth direction respectively. Even very long ocean waves with 1 km wavelength have phase speeds of less than 50 ms^{-s} (compare eq. 4-5). This means that for the spaceborne systems considered in this study the ratio of ocean wave phase speed c_{ph} and platform velocity V is very small (< 0.01) and thus the scanning distortion effect can be neglected.

4.3.4.2. “Train off the track effect”

The second mechanism to be taken into account is the so called “train off the track” effect, which is caused by Doppler frequency shifts introduced by the orbital motion of the waves. Due to the special SAR processing technique, which is based on the recording of the Doppler frequencies, this effect causes distortions of the interferogram.

According to *Bao et al.* [1997] and *Schulz-Stellenfleth & Lehner* [2001a] the interferogram i acquired over a sea surface with orbital velocity in range direction u_r and respective acceleration a_r is given by the following expression.

$$i(x,y) = 0.5\, T_0^2 \rho_a \pi \int \frac{\sigma_0(x_1,y)}{\hat{\rho}_a(x_1,y)}\ \exp(i\Phi_{hybr}(x_1,y))\ \exp(-\frac{\pi^2}{\hat{\rho}_a^2(x_1,y)}(x - x_1 - \frac{R}{V}u_r(x_1,y))^2)\ dx_1 \quad (4\text{-}21)$$

Here, x and y are the azimuth and range coordinates, σ_0 is the normalised radar cross section, R is slant range, V is platform velocity, T_0 is SAR integration time and $\hat{\rho}_a$ is the degraded azimuthal resolution given by

$$\hat{\rho}_a(x_1,y) = \sqrt{\rho_a^2 + [\frac{\pi}{2}\frac{T_0 R}{V}a_r(x_1,y)]^2 + \frac{\rho_a^2 T_0^2}{\tau_s^2}} \quad (4\text{-}22)$$

with orbital acceleration a_r, coherence time τ_s, and T_a defined as follows:

$$\frac{1}{T_a} = \frac{1}{T_0} + \frac{1}{\tau_s} \quad (4\text{-}23)$$

The basic conclusion of eq. 4-21 is that complex image points in the interferogram are shifted and smeared in azimuth direction in a similar way as known from intensity images of conventional SAR. The mechanism is called “velocity bunching” in the case of conventional SAR imagery, because it leads to a stretching and bunching of SAR image intensities *Alpers et al.* [1981]. The impact of the mechanism on the interferometric phase is slightly different, because the phases are just redistributed without changing their density *Schulz-Stellenfleth & Lehner* [2002]. We therefore prefer the term “phase mixing effect” in the context of InSAR data. An illustration of the difference of the distortions occuring in SAR intensity images and phase images is given in Fig. 4-4.

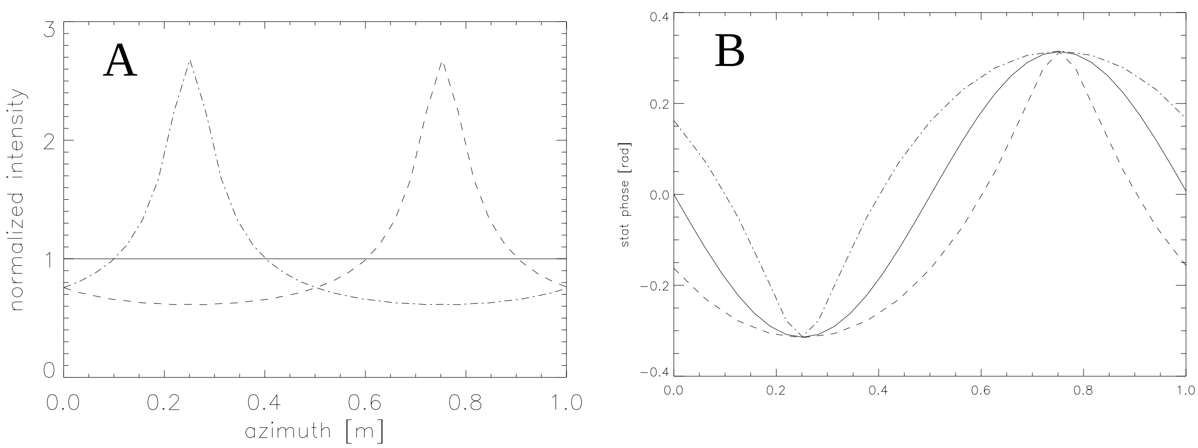

Figure 4-4: (A) SAR intensity image of a single harmonic wave for two opposite propagation directions in azimuth. (B) The same as (A) for the XTI phase. The solid line represents the phase of a stationary harmonic wave.

The dominant system parameter in the process is the ratio of slant range R and platform velocity V. It can be shown that this mechanism effectively leads to a low pass filtering of the phase spectrum in the azimuth direction *Bao et al.* [1997]; *Schulz-Stellenfleth & Lehner* [2001a].

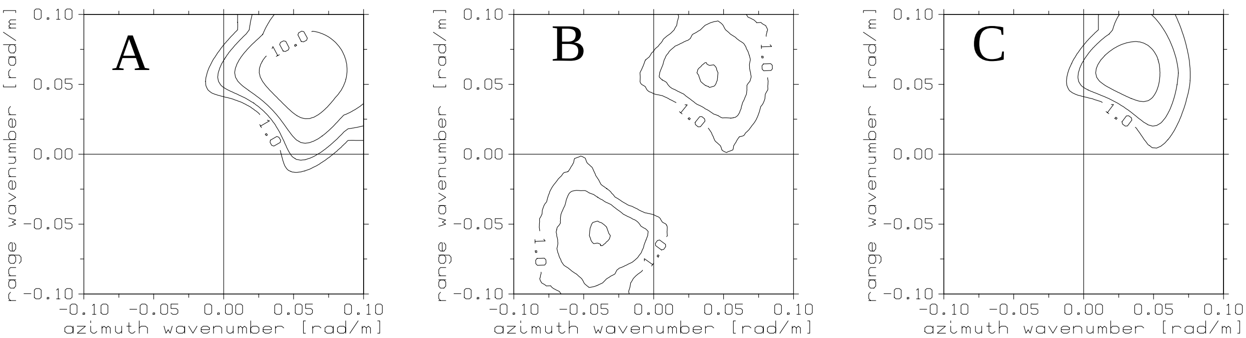

Figure 4-5: (A) JONSWAP wind sea systems, (B) XTI phase spectrum estimated using Monte Carlo simulations based on eq. 4-21, (C) XTI phase spectrum computed using the quasilinear approximation eq.4-25

4.3.4.3. Quasilinear Transform

Eq. 4-21 is a mapping relation, which relates one realization of an ocean wave field to the corresponding InSAR interferogram. Although interest has grown in the derivation ocean wave fields from remote sensing data in particular for the analysis of extreme wave events, the main focus is still on the measurement of two dimensional ocean wave spectra. To retrieve wave spectra from InSAR data integral transforms have been derived based on eq. 4-21 which allow to calculate InSAR phase variance spectra defined as:

$$P_k = |\mathcal{F}(\Phi)|^2 \tag{4-24}$$

without Monte Carlo simulations, e.g. numerically efficient. The standard approach in ocean wave spectra retrieval is based on the inversion of these integral transforms. As the complete analytical expressions are rather complicated we will only discuss the so called quasilinear approxmations, which carry the main characteristics of the full transforms. The presented transforms are taken from *Schulz-Stellenfleth & Lehner* [2002] and slightly deviate from the corresponding expression proposed in *Bao* [1993]; *Bao et al.* [1999]. The differences are due to an approximation made in the derivation of the latter exressions, which are avoided in *Schulz-Stellenfleth & Lehner* [2002].

In the quasilinear approximation the XTI phase spectrum is given by

$$P_k^{XTI} = \exp\left(-k_x^2 \frac{R^2}{V^2} \langle u_r^2 \rangle\right) \left(\frac{2\pi}{\eta^{amb}}\right)^2 \Big(F_k + F_{-k}\Big) \tag{4-25}$$

where $\langle u_r^2 \rangle$ is the variance of the orbital velocity in slant range direction. The leading exponential factor is responsible for the characteristic azimuthal cut-off. The corresponding expression for the ATI phase spectrum is given by:

$$P_k^{ATI} = \exp\left(-k_x^2 \frac{R^2}{V^2} \langle u_r^2 \rangle\right) \left(\frac{2\pi}{u_r^{amb}}\right)^2 \Big(|T_k^u|^2 F_k + |T_{-k}^u|^2 F_{-k}\Big) \tag{4-26}$$

Here T^u is the orbital velocity transfer function defined in eq. 4-16. The hybrid phase spectrum can to first order be written as:

$$P_k^{hybrid} = \exp\left(-k_x^2 \frac{R^2}{V^2} \langle u_r^2 \rangle\right) \Big(|T_k^{hyb}|^2 F_k + |T_{-k}^{hyb}|^2 F_{-k}\Big) \tag{4-27}$$

with transfer function T^{hyb} defined as:

$$T_k^{hyb} = \left(\frac{2\pi}{u_r^{amb}}\right) T_k^u + \left(\frac{2\pi}{\eta^{amb}}\right) \tag{4-28}$$

A comparison of an XTI phase spectrum estimated by Monte Carlo simulations based on eq. 4-21 and the corresponding quasi-linear approximation eq. 4-25 is shown in Fig. 4-5. It can be seen that the agreement is very good in this case. It should be said however that stronger deviations can occur in cases of stronger nonlinearities, e.g. for shorter waves propagating in the azimuth direction.

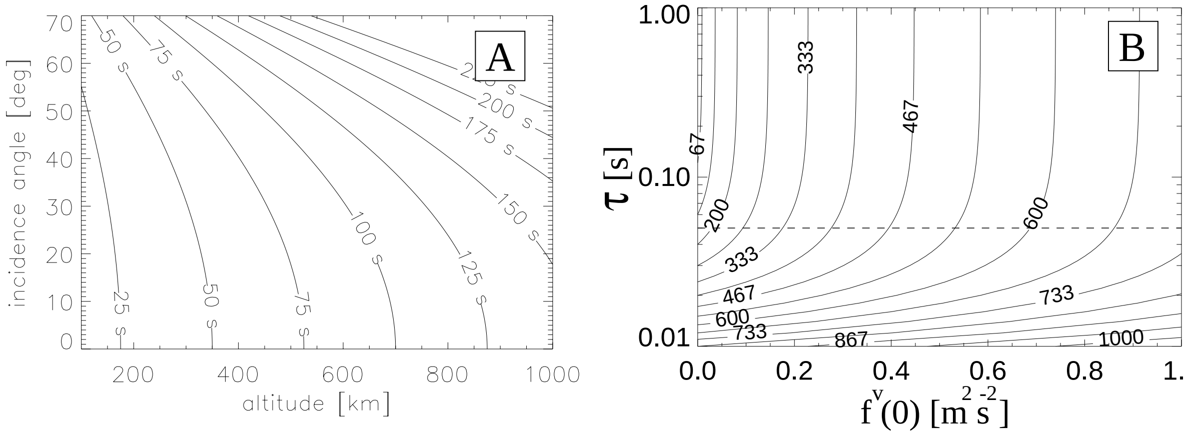

Figure 4-6: (A) The R/V ratio for spaceborne systems as a function of flight altitude and incidence angle. (B) Theoretical cut-off wavelength λ_{cut} (compare eq. 4-30) depending on coherence time τ_s and orbital velocity variance $f^v(0) = \langle u_r^2 \rangle$

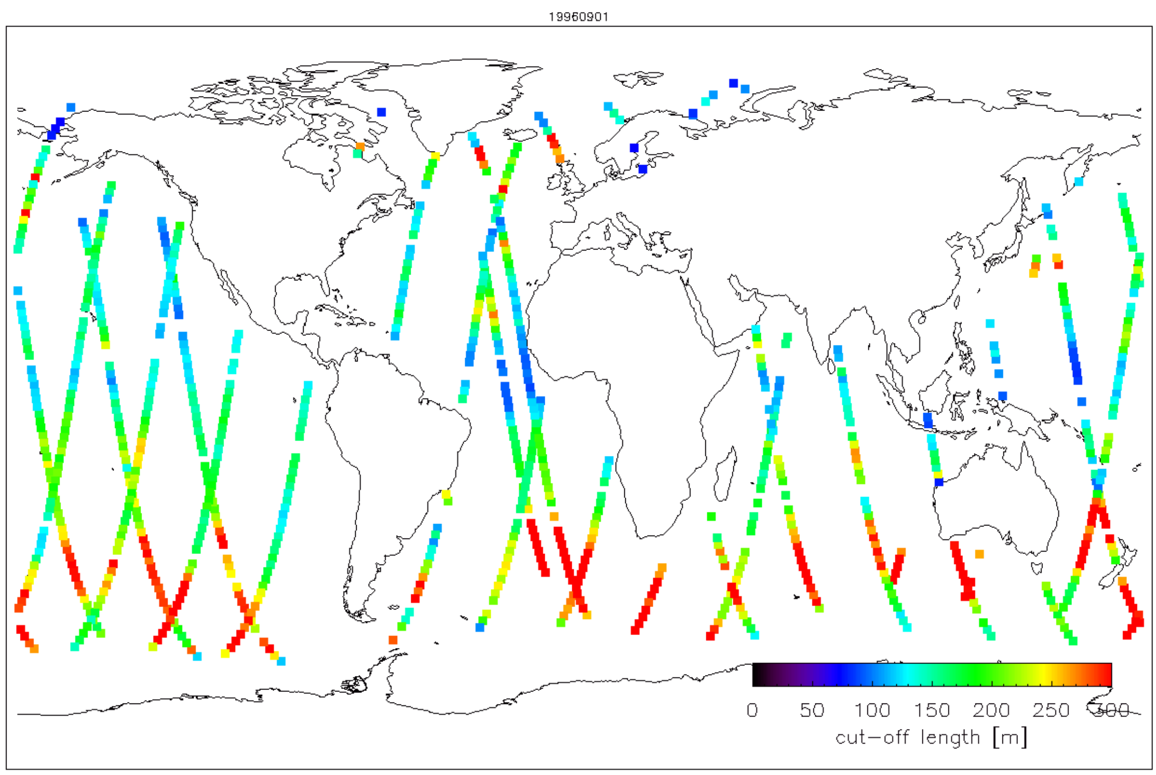

Figure 4-7: Cut-off wavelength (here defined as two times the 3dB width of the azimuth correlation function) computed from reprocessed ERS-2 SAR wave mode data acquired on Sep 1, 1996.

4.3.5. Retrieval Approaches

Due to the information loss on short waves propagating the satellite flight direction the retrieval of two dimensional wave spectra from InSAR data requires the use of some kind of prior information. This problem is already known from conventional SAR imagery and different approaches have been proposed *Hasselmann et al.* [1996]; *Mastenbroek & de Valk* [2000]; *Krogstad et al.* [1994]. The schemes use either information from wave models *Hasselmann et al.* [1996]; *Krogstad et al.* [1994] or other sensors *Mastenbroek & de Valk* [2000] to add the missing information. Retrievals are then performed using different statistical techniques like, e.g. the maximum a posteriori approach where the following cost function is minimized:

$$J(F) = \int H_k \, (P_k^{sim}(F) - P_k^{obs})^2 + G_K \, (F_k - F_k^{prior})^2 \, dk \tag{4-29}$$

Here P^{sim} is the simulated InSAR variance spectrum, F is the wave spectrum to be estimated and F^{prior} is some prior information used to add the missing information.

As the qustion of how to combine prior information and SAR information is still subject of ongoing research and out of the scope of this report we will concentrate the discussion on waves which are travelling in the approximate range direction as these cases are only weakly affected by the azimuthal cut-off.

If we futhermore replace the full nonlinear mapping relation by the quasilinear approximations introduced in section 4.3.4.3. the inversion problem becomes very simple. It consists of three main steps:

- Estimate azimuthal cut-off to identify spectral regime where information is available
- Resolve ambiguity of wave propagation direction present in phase images by applying multi-look techniques *Engen & Johnson* [1995] or using other a priori information.
- Devide phase spectrum by the corresponding transfer function (compare eq. 4-25, 4-26).

Several examples where this approach was applied to airborne InSAR data will be presented in section 4.7.

4.4. Key Parameters

4.4.1. Along Track Baseline

For the space-borne InSAR systems analysed in this study we have to consider antenna configurations with both along and across track components of the baselines. As pointed out in chapter 3 the length of the along track baseline has to be short enough to ensure sufficient coherence of the complex images acquired by the different antennas.

If the objective is to derive two dimensional ocean wave fields this limitation is more serious than for current measurements, because the correlation length of current fields is usually longer than typical ocean wave lengths. This means that for ocean wave estimation less smoothing for phase noise reduction is feasible. Fig. 4-3 shows phase standard deviations as a function of coherence for different numbers of smoothed samples *Bamler & Hartl* [1998]. For example assuming a coherence of 0.85 we have to average the interferogram down to 60 m to achieve a phase standard deviation of about 10°. If we further assume a typical spatial resolution of 20 m for a spaceborne system this smoothing is only feasible if no waves shorter than 120 m are present.

However, in most applications one is not so much interested in heights of individual waves but in the ocean wave spectrum and its integral parameters like significant wave height. For this kind of application the coherence requirements are easier to meet. We will analyze the dependence of the signal to noise ratio in phase spectra, which are the basis for wave spectra measurements in section 4.6.

4.4.2. R over V Ratio

Fig. 4-7 shows azimuthal cut-off wavelength estimated from ERS-2 wave mode intensity images, which are affected by an analogue mechanism. The reprocessed data set is described in more detail in *Lehner et al.*

[2000]. The cut-off is here defined as two times the 3dB width of the azimuthal autocorrelation function. One can see that for the ERS-2 case, which has an R/V ratio of about 110 s the highest cut-off wavelength of up to 300 m are found in regions of high sea states. e.g. in the South Atlantic. It can be shown that the cut-off wavelength increases linearly with the standard deviation of the orbital velocity of the sea surface. As the short wind generated waves have particularly strong impact on the orbital motion, the cut-off has a significant dependence on wind speed *Kerbaol et al.* [1998]. Fig. 4-6 shows the R/V ratio for spaceborne systems as a function of incidence angle and flight altitude. Approximate cut-off wavelength for systems with different R/V ratio can be obtained by multiplying the values in Fig. 4-7 with $R\,V^{-1}\,(110s)^{-1}$

A theoretical cut-off wavelength is sometimes used in the literature *Mastenbroek & de Valk* [2000]; *Kerbaol et al.* [1998] defined by:

$$\lambda_{cut} = 2\,\pi\,\sqrt{(\frac{R}{V})^2\,f^v(0) + \frac{\hat{\rho}_a^2}{4\,\pi^2}} \tag{4-30}$$

It has been shown in *Schulz-Stellenfleth & Lehner* [2001b] that this theoretical cut-off wavelength is approximately two times the empirical cut-off wavelength shown in Fig.4-7. This theoretical parameter gives insight into the dependence of the cut-off wavelength on the R over V ratio and integration time T_0 as well as the orbital velocity variance $f^v(0) = \langle u_r^2 \rangle$ and the coherence time τ_s. Fig. 4-6 (B) shows the theoretical cut-off wavelength as a function of coherence time and orbital velocity variance assuming an integration time of 1 s typical for spaceborne SAR systems. It can be seen that at least for coherence times larger than 50 ms the cut-off wavelength is dominated by the orbital motion and hence the high frequency part of the ocean wave spectrum.

4.4.3. Image Size

In order to estimate InSAR phase variance spectra properly, e.g. with low variance of the estimator, the size of the interferograms has to be sufficiently large. The achievable accuracy of the spectral estimator is depending on the spectral resolution ρ_k, which is directly connected to the image size d (for simplicity only one dimension is considered) via

$$\rho_k = \frac{2\pi}{d} \tag{4-31}$$

because at higher resolutions more smoothing is possible.

As swell waves up to 1 km wavelength can be observed the interferogram has to be at least 1 by 1 km in size. In order to obtain a decent resolution in wavelength and wave propagation direction for these longer waves the size should be 5 by 5 km or larger. In the case of the ERS-1/2 SAR wave mode imagettes of 10 by 5 km size were acquired every 200 km along the track, which turned out to be a good compromise.

4.5. Simulations of InSAR phase spectra

To analyse the ocean wave imaging capability of spaceborne InSAR systems simulations based on the forward model 4-21 are performed. In this section only the information loss and the distortions due to the nonlinear imaging mechanism is investigated without taking into account signal to noise considerations.

The ambiguity heights and velocities used for the simulations presented in this section are irrelevant for the shape of the simulated phase spectra. Simulations for different values of η^{amb} and u_r^{amb} can be obtained by simply rescaling the spectra accordingly.

For wind sea cases the simulations are based on the parametric JONSWAP model eq. 4-7. For swell a simple Gaussian shaped function is used, which has a stronger peakedness than wind seas. Phase image spectra are simulated using a Monte Carlo approach. For a given two dimensional spectrum realizations of the sea surface are computed assuming uniformly distributed phases of the harmonic components *Komen et al.* [1994]. Phase image variance spectra are estimated by averaging 50 simulations.

Fig. 4-8 shows a simulation for a swell system with 2 m waveheight which is modelled by a simple Gaussian shaped function (A). The simulated XTI and ATI phase variance spectra assuming an ambiguity height of 100 m, an ambiguity velocity of 30 ms^{-1}, a R over V ratio of 110 s and an incidence angle of 25° are shown in Fig. 4-8 (C), (D). It can be seen that for this swell case, which is characterised by a slow orbital motion, there are hardly any distortions of the phase spectrum visible. In particular the azimuthal cut-off wavelength is so short (about 100 m) that no information on the swell is lost. Due to the shape of the transfer function T_u (compare eq. 4-16), which amplifies the spectral energy of shorter waves, the peak of the ATI phase spectrum is slightly shifted towards higher wavenumbers. An estimate of the wave spectrum spectrum can be readily obtained by dividing the ATI spectrum by T_u.

A case with higher orbital velocities and hence stronger nonlinear effects is shown in Fig. 4-9. Phase image spectra for XTI and ATI configuration are simulated using the same imaging parameters as in Fig. 4-8. To illustrate the strong nonlinear distortions which can occur, a fully developed wind sea system with 150 m wavelength propagating in the exact azimuth direction is used as input for the Monte Carlo simulation. The respective XTI and ATI phase spectra are shown in Fig. 4-9 (B) and (C). It can be seen that both spectra are heavily distorted due to the “train off the track” effect described above. It is clear that for these cases a reconstruction of the original wave spectrum from the InSAR measurement is not straightforward. An analogue problem occurs in wave measurements with conventional SAR imagery and is commonly solved using prior information, e.g. from ocean wave models *Hasselmann et al.* [1996].

Fig. 4-10 shows a simulation with the same wind sea system as in Fig. 4-9 but this time with propagation direction in the exact range direction of the sensor. Monte Carlo runs were carried out for ATI-, XTI- and hybrid phase image spectra assuming the same imaging parameters as in Figs. 4-8, 4-9. It can be seen that although the spectra are low pass filtered in the azimuth direction the distortions are less severe than in the azimuth travelling case. Again the peak of the ATI phase spectrum is slightly shifted towards higher wavenumbers. Fig. 4-8 (D) shows the respective simulation for a hybrid XTI/ATI system. As can be seen the hybrid spectrum has the same characteristic cut-off as the ATI and XTI spectrum with a peak wavenumber which is slightly shifted towards higher wavenumbers.

Further simulations of across track phase spectra, which show the low sensitivity of these data with respect to modulations of the radar cross section as well as the advantages compared to conventional SAR image variance spectra can be found in *Schulz-Stellenfleth & Lehner* [2001a].

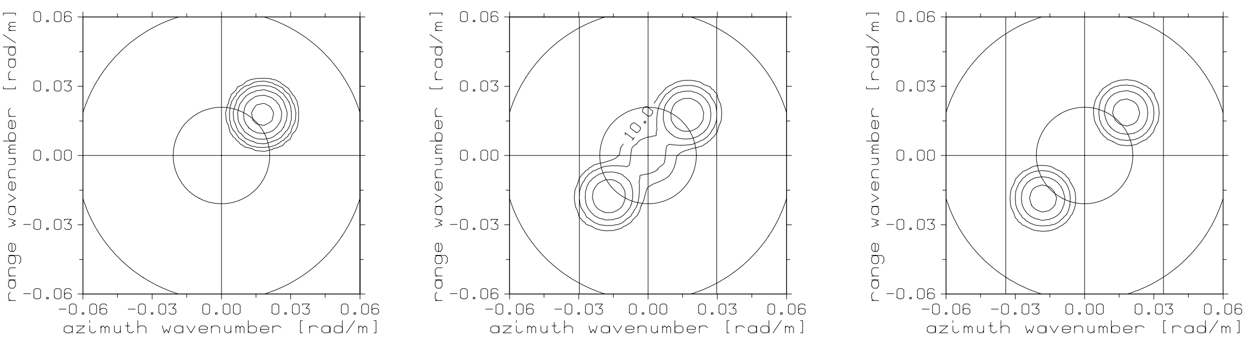

Figure 4-8: Simulation of an XTI (centre) and ATI (right) phase image spectrum using a Gaussian shaped swell spectrum with 2 m waveheight and 250 m wavelength as input. An ambiguity height of 100 m, an ambiguity velocity of 30 m and a R over V ratio of 110 s was assumed.

4.6. Signal to noise ratio of phase spectra

In this section signal to noise ratios of phase image spectra acquired by spaceborne InSAR systems are analysed. The signal to noise ratio is the most crucial parameter for the detectability of ocean wave systems in InSAR data. We will show how the noise level in the phase spectrum depends on the system resolution, the coherence and the ambiguity height and velocity respectively. Explicit signal to noise ratios are calculated for typical sea states and system parameters.

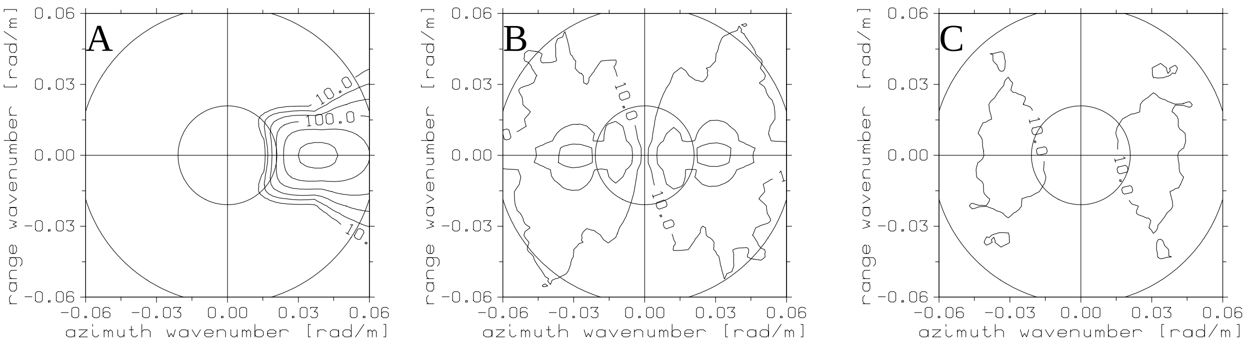

Figure 4-9: Simulation of an XTI (centre) and ATI (right) phase image spectrum using a fully developed JONSWAP wind sea with 150 m wavelength in the exact azimuth direction as input. An ambiguity height of 100 m and an ambiguity velocity of 30 m was assumed.

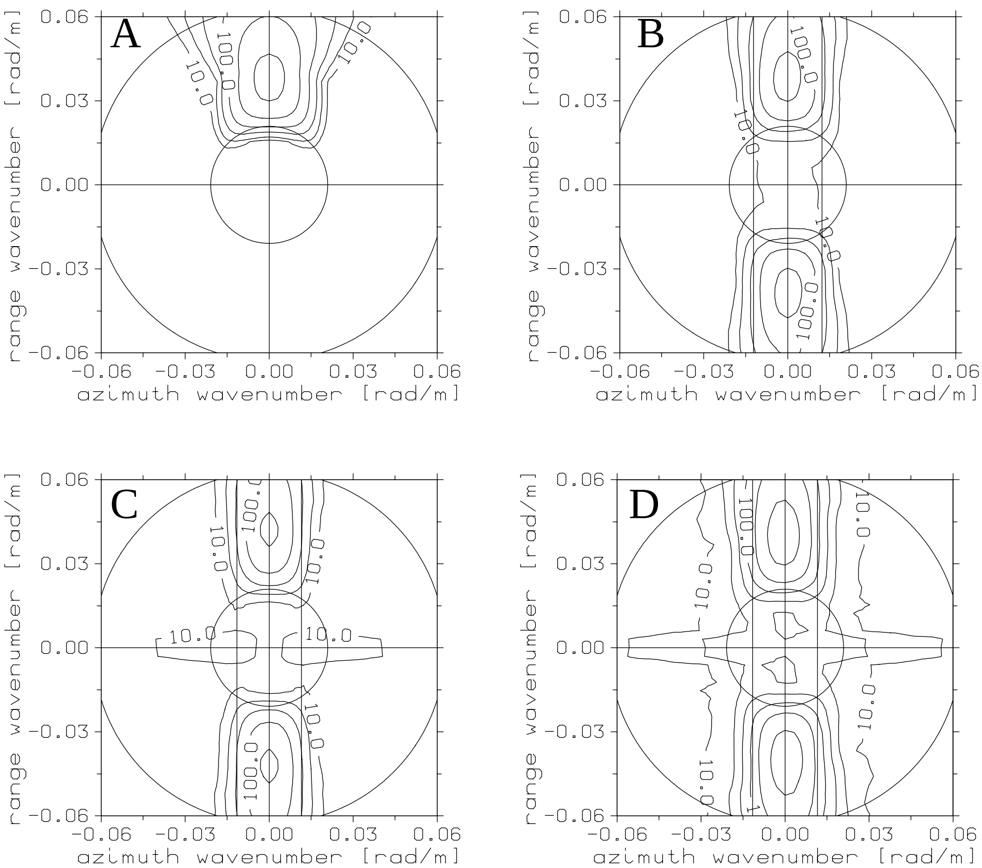

Figure 4-10: Simulation of an XTI (B), ATI (C) and hybrid phase image spectrum (D) using a fully developed JONSWAP wind sea with 150 m wavelength propagating in the exact range direction as input. An ambiguity height of 100 m and an ambiguity velocity of 30 m was assumed.

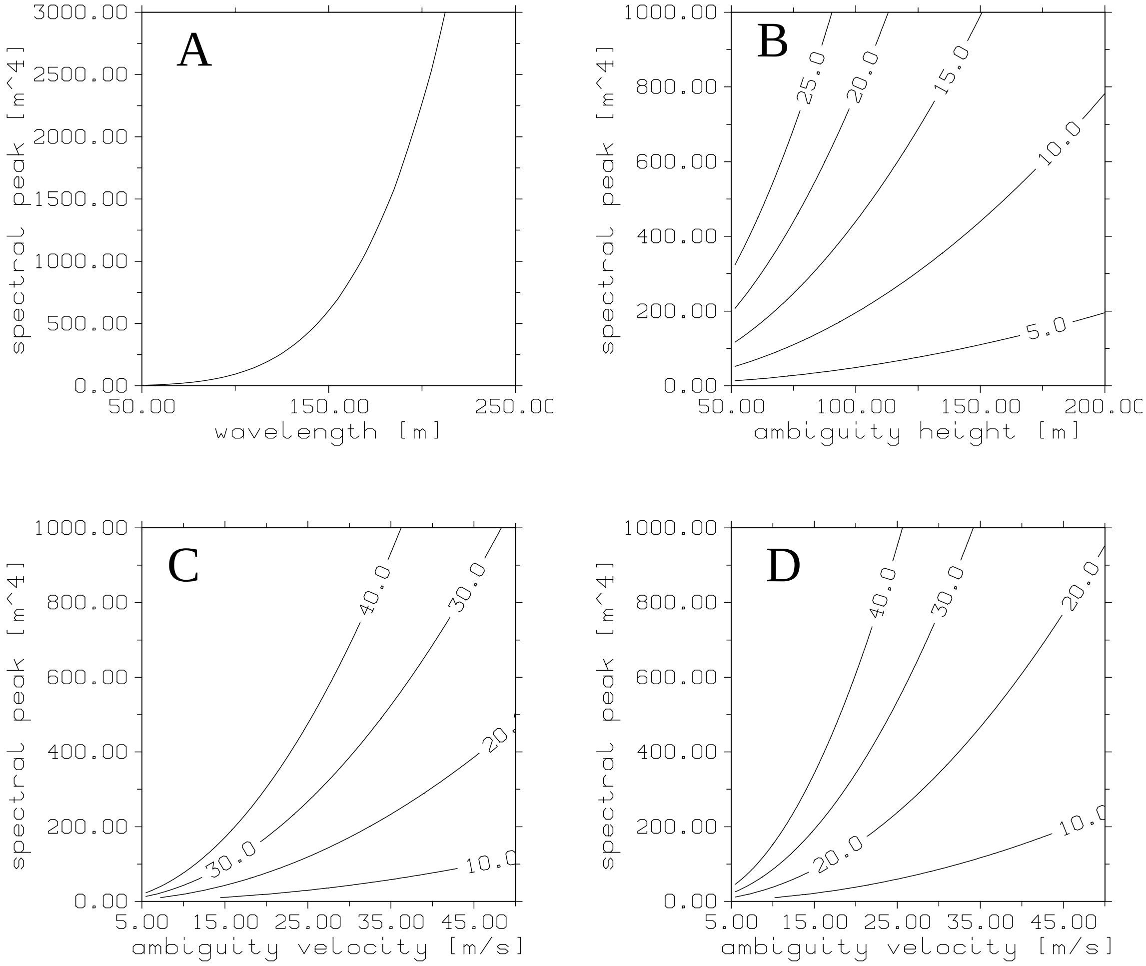

Figure 4-11: (A) Peak spectral density of a fully developed wind sea as a function of wavelength (B) Ambiguity heights and spectral peak densities for which the across track phase image spectrum has a signal to noise of 3dB assuming different phase standard deviations (given in degree). (C,D) The same as (B) for the along track phase spectrum assuming a wavelength of 150 m (C) and 300 m (D) (infinite deep water).

The analysis is based on a simple noise model for the phase image spectrum. We assume phase noise to be additive, e.g. denoting the noise-free phase with Φ_0 the measured phase Φ is given by:

$$\Phi(x) = \Phi_0(x) + n(x) \tag{4-32}$$

where n represents phase noise, which is assumed to be a white zero mean process. We know that the variance of the noise is a function of coherence *Bamler & Hartl* [1998]. Furthermore it has been shown that the coherence in turn is influenced by both the scattering process and the signal to noise ratio of the SAR intensity image. Separating both mechanisms the coherence can be written as *Bamler & Hartl* [1998]:

$$\gamma = \gamma_{SNR}\, \gamma_{sc} \tag{4-33}$$

with γ_{sc} representing decorrelation effects due to the scattering process and γ_{SNR} defined as:

$$\gamma_{SNR} = \frac{1}{1 + N_i/S_i} \tag{4-34}$$

Here N_i represents thermal and quantisation noise in the SAR intensity image and S_i is the respective signal, which is a linear function of the normalised radar cross section σ_0 of the sea surface.

$$S_i \sim \sigma_0 \tag{4-35}$$

Eq. 4-34 makes clear that it is desirable to have a radar cross section as high as possible to reduce interferometric phase noise. This fact e.g. favours VV polarised systems compared to HH system, because VV polarisation gives higher radar return given the same wind speed *Hasselmann et al.* [1985].

As the radar cross section is modulated by the long ocean waves the variance of the noise $< n^2(x) >$ is modulated accordingly. We therefore write n in the following form:

$$n(x) = n_0(x)\, S_0\, (1 + S(x)) \tag{4-36}$$

Here n_0 is a white zero mean process with unit variance, S_0 is the mean noise standard deviation and S is a zero mean process describing the modulation of the standard deviation. Using eq. 4-32 and eq. 4-37 the covariance function of the phase Φ can be calculated as

$$\rho_\Phi(x) = \rho_{\Phi_0}(x) + h(x)\, S_0^2\, (1 + \rho_S) \tag{4-37}$$

where h is the system impulse response function. Assuming that the correlation length of S is large compared to the system resolution eq. 4-37 can be approximated as:

$$\rho_\Phi(x) \approx \rho_{\Phi_0}(x) + h(x)\, S_0^2\, (1 + \langle S^2 \rangle) \tag{4-38}$$

Furthermore assuming for simplicity a box shaped system transfer function the phase variance spectrum then follows as:

$$P_\Phi = P_{\Phi_0} + S_0^2\, (1 + < S^2 >)\, \frac{\rho_a\, \rho_r}{4\, \pi^2} \tag{4-39}$$

with azimuth and range resolution given by ρ_a, ρ_r.

For our simulations we assume a modulation variance of 0.25, which is regarded as typical for moderate sea states *Brüning et al.* [1990]. A more detailed analysis of S is difficult because the different real aperture radar modulation mechanisms are known only with low accuracy *Feindt et al.* [1986]. However one should be aware that a stronger modulation variance increases the noise level of the phase spectrum. This fact again favours VV polarised systems as the modulation depth in VV polarisation is known to be smaller than in HH polarisation *Alpers et al.* [1981].

The noise model eq. 4-39 was used to analyse the dependence of the signal to noise ratio on system parameters and phase noise for both ATI and XTI spectra. Fig. 4-11 shows ambiguity heights and spectral peak densities which lead to a signal to noise ratio of 3dB for different phase standard deviations. For simplicity we have restricted the analysis to waves propagating in the exact range direction, which represents the optimal situation. For waves with azimuth component the signal to noise ratio is lower due to the azimuthal cut-off mechanism explained above. E.g. assuming a 150 m ambiguity height and a spectral peak of 400 m^4 less than 10° standard deviation are required to ensure an acceptable signal to noise ratio. The peak densities for fully developed wind seas as a function of wavelength are shown in Fig. 4-11 (B). The respective plots for along track interferometry are shown in Fig. 4-11 (C) and (D) assuming 150 m wavelength (C) and 300 m wavelength (D) respectively.

The plots can also be used to compare signal to noise ratios of ATI and XTI phase spectra for particular wave systems. Imagine a wave system of 150 m wavelength with a peak spectral density of 400m^4. Further assume that we have a phase standard deviation of 20°. Using Fig. 4-11 (B) and (C) it can then be deduced that an ambiguity height of about 70 m and an ambiguity velocity of about 50 ms^{-1} are required to ensure an acceptable signal to noise ratio in both the ATI and XTI phase spectra.

4.7. Experimental evidence

In this section experimental results obtained with airborne and spaceborne interferometric SAR systems are presented, which show the potential and limitations of this techniques with respect to ocean wave measurements.

4.7.1. Across track Interferometry

The ocean wave imaging capability of an across track InSAR system was demonstrated in the **S**AR **I**nterferometry **E**xperiment for validation of Ocean **Wave** Imaging Models (SINEWAVE), which is described in detail in *Schulz-Stellenfleth et al.* [2001].

The SINEWAVE experiment was carried out in the North Sea 11 nm west of the island Heligoland on February 12, 1998. In the experiment the ocean surface was imaged by the AeS-1 across track InSAR system with simultaneous measurements of two dimensional ocean wave spectra by a directional wave rider buoy. A photo of the twin-engined Aircommander airplane used as platform for the InSAR with some of the onboard electronics is shown in Fig. 4-12. In the experiment the airborne interferometric SAR system AeS-1 *Moreira* [1996] with two antennas mounted in across track configuration was used. The system operates at X-band with HH-polarization and 45° incidence angle.

In Fig. 4-13 the measured 2d buoy spectrum (A) is shown together with wave spectra estimated from across track InSAR data acquired at two different flight levels (1200 m, 3000 m). All three spectra are given in the range azimuth reference system of the InSAR. To make the isolines and grey values of the buoy spectrum and the symmetric bunched DEM spectra comparable, the left plot (A) shows the ocean wave spectrum divided by two. One can see that for the 1200 m case (B) the wave system visible in the bunched DEM spectrum is slightly rotated anticlockwise. The energy levels and the shape of the wave system is in good agreement with the buoy spectrum. For the 3000 m flight level the impact of the bunching mechanism is stronger. The wave system visible in the bunched DEM is exactly in the range direction, which is about 30° anticlockwise with respect to the buoy spectrum. This observation can be explained by a higher R/V ratio of about 40 s at 3000 m height compared to about 15 s at 1200 m height. Note, that peak rotations of more than 30° (depending on the local wind field) were also detected in spectra of X-band SAR intensity images acquired during the SIR-C/X-SAR mission *Melsheimer et al.* [1998].

4.7.2. Hybrid Interferometry

4.7.2.1. Hybrid two antenna interferometry from space

The capability of spaceborne InSAR systems to image ocean waves has been demonstrated using data acquired during SRTM (Shuttle radar topography mission) in February 2000. During the SRTM mission which took place between Feb 11 and Feb 22, 2000 interferometric data were acquired on a global scale using the first spaceborne single-pass SAR interferometer. The SRTM system flown on the space shuttle had a bistatic InSAR system with the receiving antenna mounted on a 70 m long mast and the transmitting antenna installed in the cargo bay. The system acquired data in both X and C band, however only C-band data were available for our study. The imaging attitude of the system in space is shown in Fig. 4-15 (B). The main goal of the mission

Velocity V	70 - 100 m/s
Height	400 m - 3000 m
Transmitting frequency	9.5 GHz
Pulse repetition frequency	8000 Hz
V-Baseline B_z	-1.3034 m
H-Baseline B_x	-1.3034 m
Incidence angle α	$20° - 80°$
Polarization	HH
Range resolution ρ_r	ca. 0.5 m
Azimuth resolution ρ_a	10 m
Integration time T_a	0.02 - 0.1 s
R/V	5 s - 70 s

Figure 4-12: (Left) Photo of the Aircommander airplane used as platform for the AeS-1 InSAR system during in the SINEWAVE experiment. Parts of the onboard radar electronics are shown in front.(B) Table with the most relevant parameters of the AeS-1 system as flown during the SINEWAVE experiment. (adapted from Schulz-Stellenfleth et al. *[2001])*

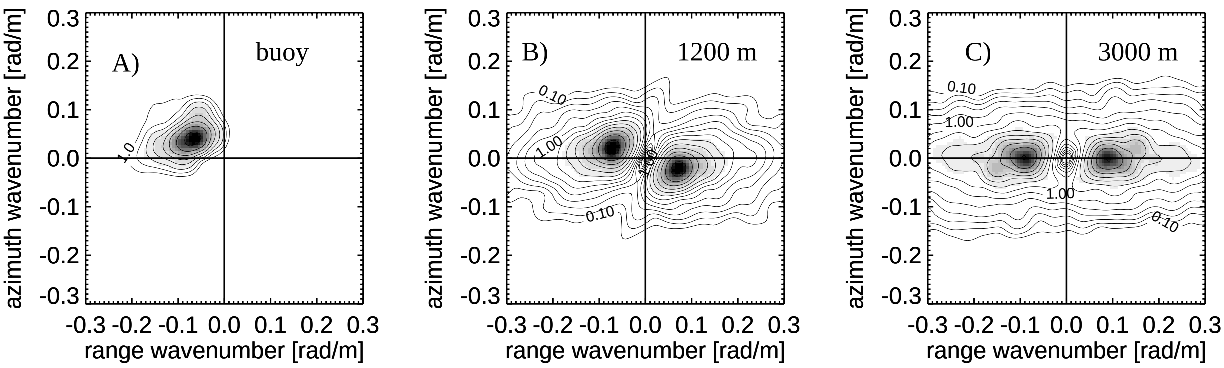

Figure 4-13: (A) Buoy spectrum (divided by two) in the range-azimuth reference system of track 1200m-07. (B) Bunched DEM spectrum of track 1200m-07. (C) Bunched DEM spectrum of track 3000m-07 (adapted from Schulz-Stellenfleth et al. *[2001]).*

was the derivation of a global digital elevation model (DEM) of high precision (about 5 m relative accuracy) over land.

Although the mission was originally devoted to pure land application the system had a an additional along track baseline component of about 7 m due to technical reasons. As it turned out now this along track baseline allows estimation of orbital velocities associated with ocean surface gravity waves and currents. Fig. 4-15 (A) shows the expected interferometric SRTM phase (C-band) as a function of orbital velocity in slant range u_r and sea surface elevation η.

Fig. 4-14 (A) shows a phase image of 3 by 3 km size which was acquired near the California Coast (120°W31°N) on Feb 17 at 17:55 UTC. The image is orientated with flight direction (35.6°) upwards. The contour-plot of the corresponding phase spectrum shown in Fig. 4-14 (B) shows an ocean wave system of about 300 m wavelength. A more detailed analysis presented in *Bao et al.* [2001] showed that the wave patterns are in fact associated with a swell wave. It turned out that interferometric phase is dominated by the along track component of the baseline, which means that the phase modulation are mainly due to variations in the orbital velocity associated with the swell system.

The SRTM data represent the first demonstration of the ocean wave imaging capability of spaceborne InSAR systems. Taking into account the system is by no means optimised for this kin of application, the obtained results are very promising at least concerning along track interferometry.

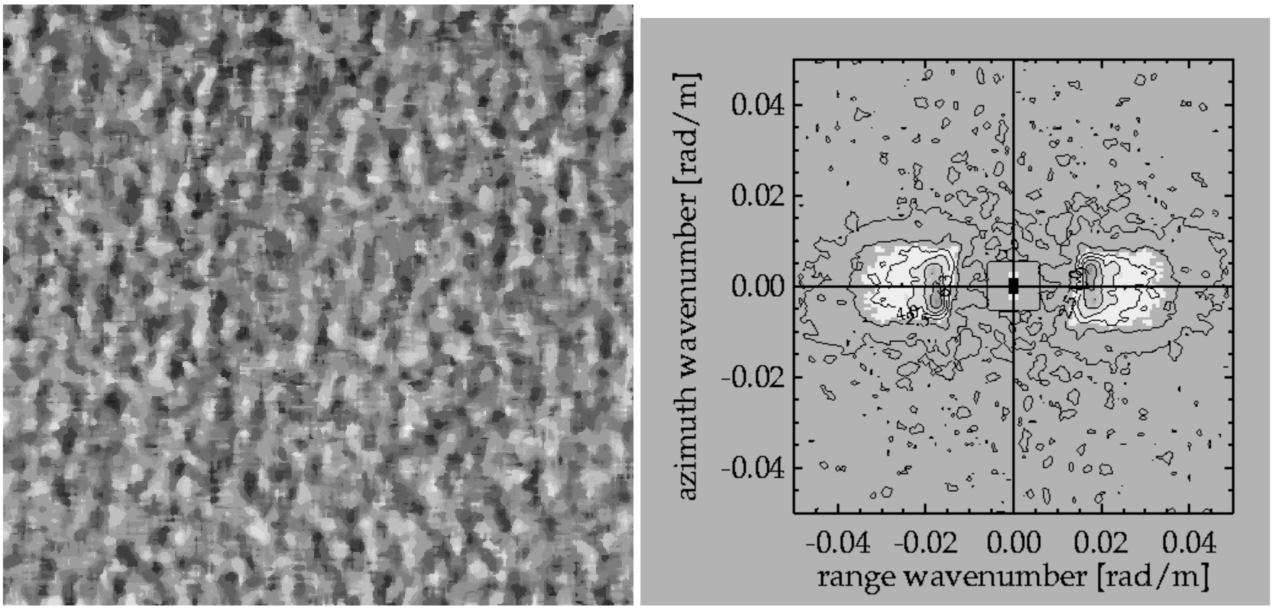

Figure 4-14: (A) SRTM phase image of 3 by 3 km size acquired near the California Coast (120°W31°N) on Feb 17 at 17:55 UTC (B) Corresponding phase image variance spectrum

4.7.2.2. Airborne three antenna hybrid interferometric measurements

In this section we will demonstrate how a three antenna interferometric SAR system can be used to decouple along and across track components. This technique allows to separate the phase component associated with sea surface elevation in cases where no interferometric pair with pure across track baseline is available. The method could e.g. be applied to data acquired by an interferometric cartwheel with three receiver satellites. The technique is illustrated using airborne data acquired during the GIJON experiment which was carried out in the framework of the EuroROSE project funded by the European Union.

The Gijon experiment took place in the Golf of Biscay on Nov 9, 2000. Ocean wave and current measurements were carried out by different sensors near the coast between the harbour of Gijon and Cabo de Penas. Apart from the InSAR acquisitions collocated measurements were performed by ground-based marine radar, HF radar, buoys and the European remote sensing satellite ERS-2.

As in the SINEWAVE experiment the airborne AeS-1 system developed by Aerosensing GmbH was used in the

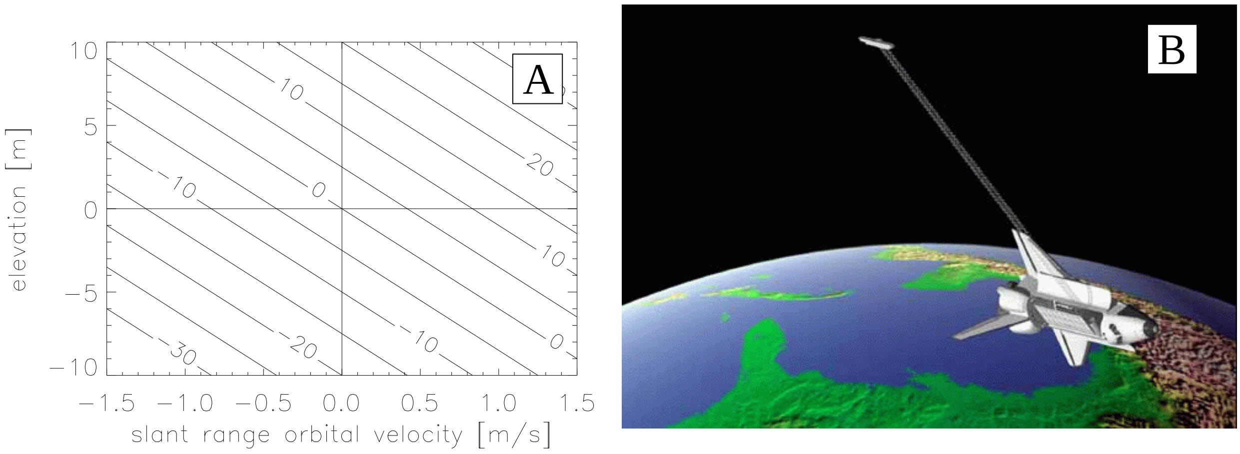

Figure 4-15: (A) SRTM interferometric phase in degree as a function of sea surface elevation η and orbital velocity in slant range u_r. (B) Space shuttle with mounted interferometric system during the SRTM mission.

Gijon experiment. However this time the system was flown using three antennas with a geometry as indicated in Fig. 4-16 (left). A speciality of the AeS-1 system is the ability to operate in monostatic (antennas transmit and receive separately) and bistatic modes (only one antenna transmits) simultaneously. For the system used in the Gijon experiment both the master and the first slave antenna were able to either transmit or receive signals. Effectively this means that additional (virtual) antennas as indicated in Fig. 4-16 (right) are available for interferometric measurements.

The pure along track combination $M - S_1$ (compare Fig. 4-16 (right) had an ambiguity velocity of about 5ms^{-1} (in bistatic mode), which allows measurements of orbital velocities with high accuracy. Fig. 4-18 shows a two dimensional wave spectrum as estimated from the along track data in comparison with the collocated marine radar measurement. The R over V ratio, which is the dominating imaging parameter was 40 s in this case. It can be seen that wavelength, waveheight as well as wave propagation direction are in good agreement.

To extract the sea surface elevation information contained in the across track combinations $M - S_2$, $S_1 - S_2$ a technique which is described in more detail in *Lehner et al.* [2002] was applied. The basic idea is that a multi-antenna system provides a set of equations of the form 4-18, which has a unique solution for the orbital velocity u_r and the elevation η as long as the coefficients, which are determined by the imaging geometry, meet certain criteria.

In Fig. 4-17 the technique is demonstrated using data acquired at 1500 m flight level with an R over V ratio of 25 s and an ambiguity height of 35 m. The derived sea surface elevation and orbital velocity fields of about 400 x 400 m are shown in (C) and (D). Waves of about 150 m wavelength are clearly visible in both images. The amplitude image as well as one of the original phase images processed from the antenna combination $M - S_2$ are shown in Fig. 4-17 (B) and (E). Diagonal cuts through the the phase images used as input are shown in Fig. 4-17 (A). The significant waveheight directly estimated from the derived sea surface elevation field is about 2.5 m and thus in good agreement with ground based measurements of about 2.3 m.

In summary one can say that the proposed technique opens up a new approach to ocean wave measurements with simultaneous and independent estimates of sea surface elevation and orbital velocity. The technique is in principle applicable to spaceborne SAR data, e.g. acquired by an interferometric cartwheel. However taking into account that the (global) average significant waveheight is about 2.5 m, which means an amplitude standard deviation of about 0.6 m it is obvious that extreme accuracies are required to deal with medium sea states. It is still interesting however to think about observations of extreme sea states, which can generate individual waves of 30 m height and more.

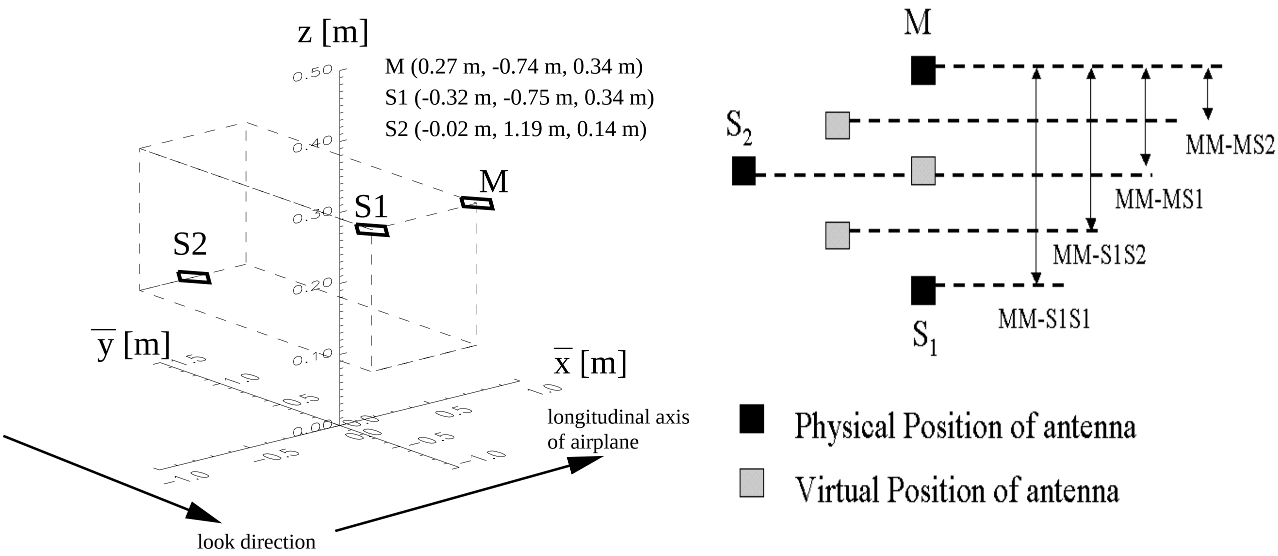

Figure 4-16: (Left) Three antenna configuration of AeS-1 InSAR system used in the Gijon experiment. (Right) The AeS-1 system can be operated in monostatic and bistatic modes simultaneously. Effectively this means that three additional (virtual) antennas can be used for interferometry.

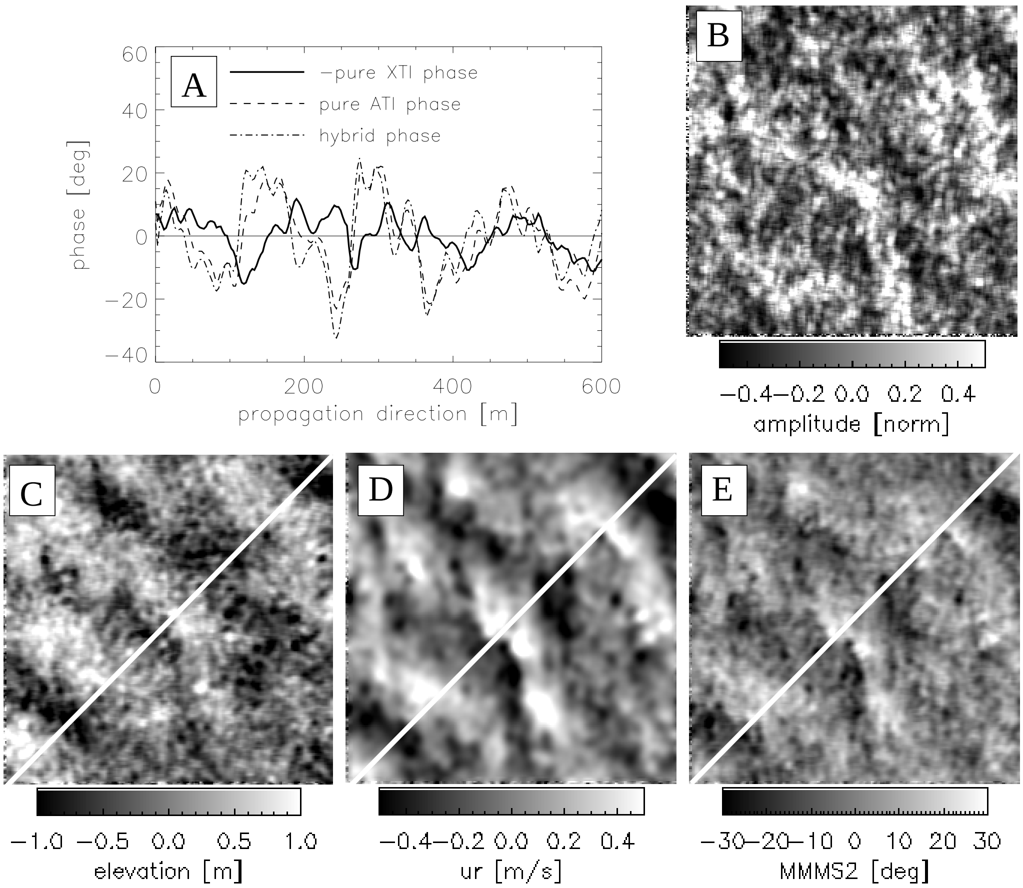

Figure 4-17: Interferometric data acquired by the AeS-1 system during the Gijon experiment at track bb02-05.

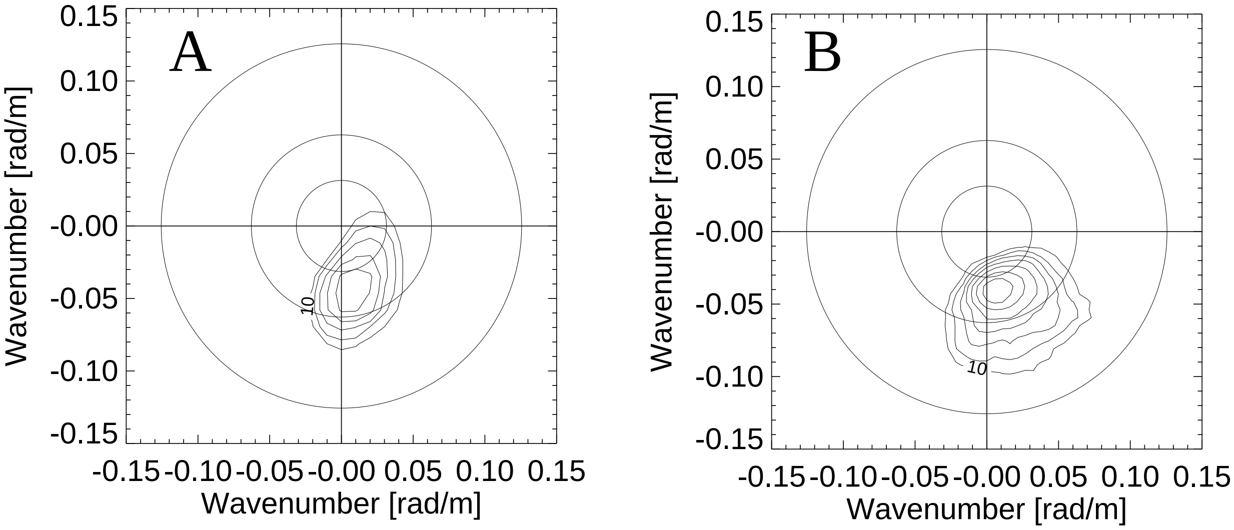

Figure 4-18: (A) Two dimensional wave spectrum with 2.7 m waveheight derived from airborne interferometric along track data. (B) Collocated wave spectrum measured by the marine radar WAMOS.

4.8. SUMMARY

A study was presented which analyses the capability of spaceborne InSAR systems to provide information on ocean waves.

Theoretical as well experimental results were presented which show the basic potential and limitations of the technique. The main conclusions are:

- The SRTM mission has proved the ability of spaceborne InSAR systems to image ocean waves.
- Spaceborne InSAR data are affected by an azimuthal cut-off similar to conventional SAR imagery. Defining the cut-off wavelength as two times the azimuthal autocorrelation function it is on average not possible to detect waves propagating in flight direction shorter than 150 m. The cut-off wavelength can increase up to 300 m in heavy sea states.
- In order to minimize the azimuthal cut-off wavelength low platform altitudes and small incidence angles are favourable.
- Due to the decorrelation of the sea surface interferometric measurements of ocean waves are only possible if the along track baseline does not exceed a certain limit, which is depending on radar frequency and wind conditions. For ocean wave measurements this side condition is in general more critical than for the current measurements descibed in chapter 3, as less smoothing for phase noise reduction is possible.
- Across track interferometric measurements of ocean waves are a challenge as they require a (relative) height resolution of certainly less than 5 m to resolve average sea states. However, the measurement of extreme sea states is still an interesting application even for systems which do not meet this requirement.
- To minimize phase noise it desirable to have high radar cross sections. This requirement favours systems with VV polarisation.
- VV polarisation has the additional advantage of weaker radar cross section modulation than HH polarisation. It was shown this fact leads to lower noise levels in the interferometric phase spectra.
- Experiments with airborne three antenna systems have shown the possibility to separate along and across track components allowing to obtain independent measurements of sea surface elevation and orbital velocity.

- Along track interferometric data allow to resolve average sea states with feasible signal to noise ratios.
- To allow continuous ocean wave measurements on a global scale spaceborne InSAR systems should be able to operate in a mode similar the the ERS wave mode where images of 10 by 5 km size are acquired every 200 km along the track.

In summary one can say that spaceborne measurements of ocean waves are certainly possible using along track interferometry. Except for cases with very low coherence the estimated wave heights are expected to have a higher accuracy than conventional SAR measurements because the high uncertainties in the radar cross section modulation model, which are the main source of error, are mostly irrelevant for interferometry. One has to be aware however that information is lost on short waves propagating in flight direction so that the retrieval of complete two dimensional wave spectra in general requires some additional a priori information.

ACKNOWLEDGMENTS

The SINEWAVE experiment was carried out in the framework of the SARPAK project sponsored by the BMBF. The Gijon experiment was partly sponsored by the EuroROSE project funded by the European Union. The presented ERS-2 data were reprocessed from raw data kindly provided by the European Space Agency.

References

Alpers, W. R., D. B. Ross, C. L. Rufenach. On the detectability of ocean surface waves by real and synthetic aperture radar. *J. Geophys. Res.*, 86, pp. 6481–6498 [1981].

Bamler, R., P. Hartl. Synthetic aperture radar interferometry. *Inverse Problems*, 14, pp. R1–R54 [1998].

Bao, M. A nonlinear integral transform between ocean wave spectra and phase image spectra of across-track interferometric SAR. In: *Proceeding of the IGARSS 99 conference, Hamburg, Germany*, pp. 2619–2621 [1993].

Bao, M., W. Alpers, C. Brüning. A new nonlinear integral transform relating ocean wave spectra to phase image spectra of an along track interferometric synthetic aperture radar. *IEEE Trans. on Geosci. and Remote Sens.*, 357, pp. 461–466 [1999].

Bao, M., C. Brüning, W. Alpers. Simulation of ocean waves imaging by an along-track interferometric synthetic aperture radar. *IEEE Trans. on Geosci. and Remote Sens.*, 35, pp. 618–631 [1997].

Bao, M., S. Lehner, J. Schulz-Stellenfleth, M. Eineder. First results on ocean wave imaging from the shuttle radar topography mission (SRTM). In: *Proceedings of the IGARSS2001 Conference, Sydney.* [2001].

Breivik, L. A., M. Reistad, H. Schyberg, J. Sunde, H. E. Krogstad, H. Johnson. Assimilation of ERS SAR wave spectra in an operational wave model. *J. Geophys. Res.*, 103, pp. 7887–7900 [1998].

Brüning, C., W. Alpers, K. Hasselmann. Monte-Carlo simulation studies of the nonlinear imaging of a two dimensional surface wave field by a synthetic aperture radar. *Int. J. Rem. Sens.*, 11, pp. 1695–1727 [1990].

Brüning, C., R. Schmidt, W. Alpers. Estimation of ocean wave-radar modulation transfer function from synthetic aperture radar imagery. *J. Geophys. Res.*, 99, pp. 9803–9815 [1994].

Dietrich, G., K. Kalle, W. Krauss, G. Siedler. *Allgemeine Meereskunde*. Gebrüder Borntraeger [1975].

Engen, G., H. Johnson. SAR-ocean wave inversion using image cross spectra. *IEEE Trans. Geosci. Rem. Sens.*, 33, pp. 1047–1056 [1995].

Feindt, F., J. Schröter, W. Alpers. Measurement of the ocean wave-radar modulation transfer function at 35 GHz from a sea-based platform of the North Sea. *J. Geophys. Res.*, 91, pp. 9701–9708 [1986].

Goldstein, R. M., T. P. Barnett, H. A. Zebker. Remote sensing of ocean currents. *Science*, 246, pp. 1282–1285 [89].

Goldstein, R. M., F. Li, J. Smith, R. Pinkel, T. P. Barnett. Remote sensing of ocean waves: The surface wave process program experiment. *J. Geophys. Res.*, 99, pp. 7945–7950 [94].

Graber, H. C., D. R. Thompson, R. E. Carande. Ocean surface features and currents measured with synthetic aperture radar interferometry and HF radar. *J. Geophys. Res.*, 101, pp. 25,813–25,832 [1996].

Hasselmann, D. E., M. Dunckel, J. A. Ewing. Directional wave spectra observed during JONSWAP 1973. *J. Phys. Oceanography*, 10, pp. 1264–1280 [1980].

Hasselmann, K. Directional wave spectra observed during JONSWAP. *J. Phys. Oceanography*, 10, pp. 1264–1280 [1973].

Hasselmann, K., S. Hasselmann. On the nonlinear mapping of an ocean wave spectrum into a synthetic aperture radar image spectrum. *J. Geophys. Res.*, 96, pp. 10,713–10,729 [1991].

Hasselmann, K., R. K. Raney, W. J. Plant, W. Alpers, R. A. Shuchman, D. R. Lyzenga, C. L. Rufenach, M. J. Tucker. Theory of synthetic aperture radar ocean imaging: A MARSEN view. *J. Geophys. Res*, 90, pp. 4659–4686 [1985].

Hasselmann, S., C. Brüning, K. Hasselmann, P. Heimbach. An improved algorithm for the retrieval of ocean wave spectra from synthetic aperture radar image spectra. *J. Geophys. Res.*, 101, pp. 16,615–16,629 [1996].

Kerbaol, V., B. Chapron, P. W. Vachon. Analysis of ERS-1/2 synthetic aperture radar wave mode imagettes. *J. Geophys. Res.*, 103, pp. 7833–7846 [1998].

Komen, G. J., L. Cavaleri, M. Donelan, K. Hasselmann, S. Hasselmann, P. Janssen. *Dynamics and modelling of ocean waves*. Cambridge University Press [1994].

Krogstad, H., O. Samset, P. W. Vachon. Generalizations of the nonlinear ocean-SAR transformation and a simplified SAR inversion algorithm. *Atmos. Ocean*, 32, pp. 61–82 [1994].

Lehner, S., H. Guenther, L. Wyatt, J. Schulz-Stellenfleth, K. Hessner, J. Green, N. Borge, K. Gurgel, J. Horstmann. Ocean wave and current measurements with a three antenna interferometric synthetic aperture radar. *IEEE* [2002]. In preparation.

Lehner, S., J. Schulz-Stellenfleth, B. Schättler, H. Breit, J. Horstmann. Wind and wave measurements using complex ERS-2 SAR wave mode data. *IEEE, TGARS*, 38, pp. 2246–2257 [2000].

Lionello, P., H. Günther, P.Janssen. Assimilation of altimeter data in a global third generation wave model. *J. Geophys. Res.*, 97, pp. 14,453–14,474 [1992].

Mastenbroek, C., C. F. de Valk. A semi-parametric algorithm to retrieve ocean wave spectra from synthetic aperture radar. *J. Geophys. Res.*, 105, pp. 3497–3516 [2000].

Melsheimer, C., W. Alpers, M. Gade. Investigation of multifrequency/multipolarization radar signatures of rain cells over the ocean using SIR-C/X-SAR data. *J. Geophys. Res.*, 103, pp. 18,851–18,866 [1998].

Mitsuyasu, H., F. Tasai, T. Suhara, S. Mizuno, M. Ohkuso, T. Honda, K. Rikiischi. Observations of the directional spectrum of ocean wave using a clover leaf buoy. *J. Phys. Oceanography*, 5, pp. 750–760 [1975].

Moreira, J. Design of an airborne interferometric SAR for high precision DEM generation. *Int. Archives of Photogrammetry and Rem. Sens.*, XXXI, pp. 256–265 [1996].

Romeiser, R., A. Schmidt, W. Alpers. A three-scale composite surface model for the ocean wave-radar modulation transfer function. *J. Geophys. Res.*, 99, pp. 9785–9801 [1994].

Romeiser, R., D. R. Thompson. Numerical study on the along-track interferometric radar imaging mechanism of oceanic surface currents. *IEEE Trans. on Geosc. and Rem. Sensing*, 38, pp. 446–458 [2000].

Schulz-Stellenfleth, J., J. Horstmann, S. Lehner, W. Rosenthal. Sea surface imaging with an across track interferometric synthetic aperture radar (InSAR) - the SINEWAVE experiment. *IEEE Transactions on Geoscience and Remote Sensing*, 39, no. 9, pp. 2017–2028 [2001].

Schulz-Stellenfleth, J., S. Lehner. Ocean wave imaging using an airborne single pass cross track interferometric SAR. *IEEE Transactions on Geoscience and Remote Sensing*, 39, pp. 38–44 [2001a].

—. Spaceborne synthetic aperture radar observations of ocean waves travelling into sea ice [2001b]. Accepted.

—. On the mapping of two dimensional ocean wave spectra by interferometric synthetic aperture radar systems [2002]. In preparation.

Shemer, L., E. Kit. Simulation of an interferometric synthetic aperture radar imagery of an ocean system consisting of a current and a monochromatic wave. *J. Geophys. Res*, 96, pp. 22,063–22,073 [1991].

Shemer, L., M. Marom, D. Markam. Estimates of currents in the nearshore ocean region using interferometric synthetic aperture radar. *J. Geohys. Res.*, 98, pp. 7001–7010 [1993].

Siegmund, R., M. Bao, S. Lehner, R. Mayerle. First demonstration of surface currents imaged by hybrid along and cross track interferometric synthetic aperture radar. *IEEE* [2002]. In Preparation.

Werner, M. Shuttle radar topography mission (SRTM) - mission overview. In: *Proceedings of EUSAR2000, Munich, Germany* [2000].

Wimmer, C., R. Siegmund, M. Schwäbisch, J. Moreira. Generation of high-precision DEMs of the wadden sea with airborne interferometric SAR. *IEEE Trans. on Geosc. and Rem. Sensing*, 38 [2000].

Young, I., W. Rosenthal, F. Ziemer. Three dim analysis of marine radar images for the detection of ocean wave directionality and surface currents. *J. of Geophys. Res.*, 90, pp. 1049–1059 [1985].